actuators

MDPI

Article

Comparative Study on Coordinated Control of Path Tracking and Vehicle Stability for Autonomous Vehicles on Low-Friction Roads

Manbok Park [1] and Seongjin Yim [2,*]

[1] Department of Electronic Engineering, Korea National University of Transportation, Chungju-si 27469, Republic of Korea; ohnnuri@ut.ac.kr
[2] Research Center for Electrical and Information Technology, Seoul National University of Science and Technology, Nowon-gu, Seoul 01811, Republic of Korea
* Correspondence: acebtif@seoultech.ac.kr; Tel.: +82-2-970-9011

Abstract: This paper presents a comparative study on coordinated control of path tracking and vehicle stability for autonomous vehicles on low-friction roads. Generally, a path-tracking controller designed on high-friction roads cannot provide good performance under low-friction conditions. To cope with the problem, a coordinated control between path tracking and vehicle stability has been proposed to date. In this paper, three types of coordinated controllers are classified according to the controller structure. As an actuator, front-wheel steering, four-wheel steering, and four-wheel independent braking and driving are adopted. A common feature of these types of controllers is that front steering and yaw moment control are adopted as control inputs. To convert the yaw moment control into tire forces generated by combinations of multiple actuators, a control allocation method is applied. For each type, a controller is designed and simulated using vehicle simulation software. From the simulation results, a performance comparison among those controller types is carried out. Through comparison, it is shown that there are small differences among those types of controllers in terms of path tracking.

Keywords: autonomous vehicle; path-tracking control; vehicle stability control; linear quadratic regulator; control allocation; low-friction condition

Citation: Park, M.; Yim, S. Comparative Study on Coordinated Control of Path Tracking and Vehicle Stability for Autonomous Vehicles on Low-Friction Roads. *Actuators* **2023**, *12*, 398. https://doi.org/10.3390/act12110398

Academic Editors: Keigo Watanabe, Gengxiang Wang, Binghe Liu and Yongjun Pan

Received: 5 October 2023
Revised: 24 October 2023
Accepted: 24 October 2023
Published: 25 October 2023

1. Introduction

Autonomous driving has been regarded as a next-generation solution for future transportation in research groups and the automotive industry since 2010 because it can prevent several types of traffic accidents and make road safety and traffic flow better [1–3]. From the literature survey, it is widely known that a generic modular system architecture for autonomous driving comprises detection, localization, prediction, planning, and control [2]. Among those topics, path-tracking control (PTC) has been intensively studied [4,5]. Consequently, a great deal of papers have been published in the area of PTC [4–10].

The aim of PTC is to make a vehicle follow a target path. For this purpose, most of the path-tracking controllers proposed to date have tried to minimize the lateral offset error (e_y) and heading error (e_φ), which are derived from the current vehicle position and target path [8,9]. Generally, front-wheel steering (FWS) or four-wheel steering (4WS) has been adopted as a control input or an actuator of a path-tracking controller. In this paper, 4WS means the combination of FWS and rear-wheel steering (RWS). This controller has shown good performance for path tracking on high-friction roads because this is designed and tuned under high-friction conditions. However, a PTC designed on high-friction roads cannot provide good performance under low-friction conditions [11–13]. This is caused by the fact that the lateral tire force of a vehicle becomes small on low-friction roads. To cope with the problem, PTC has been integrated with vehicle stability or lateral stability

control. Vehicle stability control (VSC) has been intensively studied since the middle of the 1990s [14–17]. In this paper, VSC stands for yaw rate tracking and lateral stability controls, where the former tries to minimize the yaw rate error (γ_e) and the latter tries to keep the side-slip angle (β) as small as possible. Generally, the yaw moment control (ΔM_z) has been adopted as a control input of VSC. ΔM_z is a virtual input, which should be generated by multiple actuators installed in real vehicles. For this reason, ΔM_z is to be converted into the tire forces generated by multiple actuators. This procedure is called control allocation or yaw moment distribution. Actuators used to generate ΔM_z are FWS, 4WS, RWS, and four-wheel independent steering/driving/braking (4WIS/4WID/4WIB) [18,19]. Most control allocation methods are quadratic programming (QP) with equality or/and inequality constraints [11–13,18,19].

Numerous papers have been published on the coordinated control of path tracking and vehicle stability on low-friction road conditions [11–13,20–40]. These papers can be classified into three types. Figure 1 shows the control structures of these types.

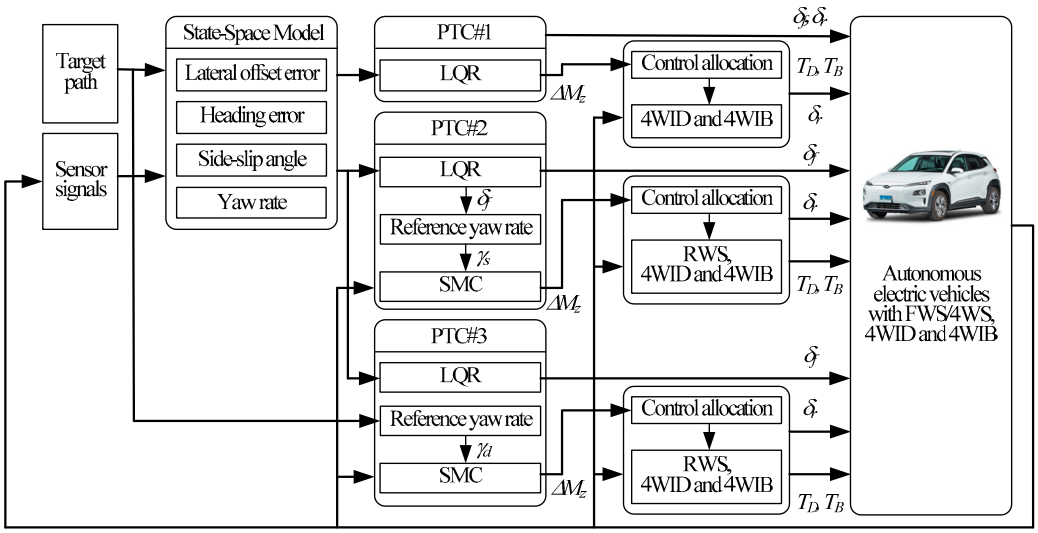

Figure 1. Structures of PTC#1, PTC#2, and PTC#3.

The first type of coordinated control method is to use two-level controllers: upper- and lower-level controllers [13,20–29]. As a control input, steering angles and ΔM_z are calculated by controllers such as model predictive control (MPC), PID control, sliding mode control (SMC), and H_∞ control in the upper-level controllers (UPLC). Among the control inputs, steering angles and ΔM_z are in charge of PTC and VSC in low-friction roads, respectively. For controller design, most of these types of controllers adopted a state-space model with e_y, e_φ, and its rates. ΔM_z is converted into tire forces generated by a single actuator or a combination of multiple ones such as FWS, RWS, 4WS, 4WIS, 4WIB, and 4WID in the lower-level controller (LWLC). For this purpose, a control allocation method was adopted. The steering angles of FWS, RWS, and 4WS, and braking and traction torques of 4WID and 4WIB are calculated from the converted tire forces. The effects of combinations of multiple actuators on path-tracking performance were deeply investigated in the previous research [13]. According to this work, there are few differences among the combinations of FWS, 4WS, 4WID, and 4WIB in terms of path-tracking performance. In other words, it is quite enough to use only FWS for path tracking. Let us denote this type of method as PTC#1.

The second type of coordinated control method is to use three-level controllers: upper-, middle-, and lower-level controllers [12,30–37]. In the UPLC, the front steering angle is calculated by a driver model or a controller. As a driver model, pure pursuit and Stanley methods have been widely used to date [4,11,12]. As a controller for steering angle generation, linear quadratic regulator (LQR), MPC, and SMC have been widely adopted with the state-space model whose state variables are e_y and e_φ. This is identical to PTC#1 with FWS. In the middle-level controller (MDLC), a reference yaw rate (γ_{ref}) is calculated from

the front steering angle (δ_f), and a controller is designed to calculate ΔM_z, which is needed to make a vehicle follow the reference yaw rate. Most of MDLCs adopted SMC in order to calculate ΔM_z. In the previous paper, the reference yaw rate is directly generated as a control input of the UPLC, H_∞ control [34]. In the LWLC, ΔM_z is converted into tire forces generated by multiple actuators. For this purpose, a control allocation method is applied. Let us denote this type of method as PTC#2. In view of PTC#1, it seems unnecessary to use the three-level controller of PTC#2 because PTC#1 has the upper- and middle-level controllers of PTC#2 in the UPLC. In other words, to generate ΔM_z, PTC#2 requires two controllers although PTC#1 does a single controller. If the path-tracking performance of PTC#2 is not superior to that of PTC#1 on low-friction roads, then PTC#2 is useless.

The third type of coordinated control method is identical to the second one except that the reference yaw rate is obtained from a target path in the UPLC [11,38–40]. In this type of method, a driver model or LQR is needed to generate δ_f. In the MDLC of this method, SMC has been applied to calculate ΔM_z, which is needed to make a vehicle follow the reference yaw rate. In the LWLC, a control allocation method was applied to convert ΔM_z into tire forces generated by multiple actuators such as RWS, 4WID, and 4WIB. Let us denote this type of method as PTC#3. In view of PTC#1, PTC#3 has the identical problem to PTC#2 because PTC#3 has a three-level structure.

The first feature of PTC#1, PTC#2, and PTC#3 is the control allocation in LWLC, which is applied to distribute ΔM_z into tire forces generated by combinations of multiple actuators. In fact, control allocation and LWLC are synonymous. For control allocation, an optimization method with QP has been applied to date. These are quite general in vehicle stability control or lateral stability control. For this reason, PTC#1, PTC#2, and PTC3 try to integrate path tracking and vehicle stability control for driving on low-friction roads.

The second feature of PTC#2 and PTC#3 is the calculation procedure of γ_{ref}. PTC#1 does not use γ_{ref}. In PTC#2 and PTC#3, γ_{ref} for path tracking is calculated from δ_f or a target path in the MDLC. In PTC#1, PTC#2, and PTC#3, δ_f is generated using LQR. Because δ_f is already determined using LQR in the UPLC, it is excluded from the control allocation procedure. In other words, δ_f is not determined using the control allocation procedure. For this reason, the actuators used for control allocation are RWS, 4WID, and 4WIB.

The third feature of these methods is to use a preview or lookahead function along the heading direction [12,21,22,24,34,38,40]. Generally, the larger the preview distance the smaller the steering angle. Especially, the preview distance should be larger for lateral stability on low-friction roads. On the contrary, the preview distance should be smaller for path tracking on high-friction roads [12,41]. For this reason, the preview distance should be carefully tuned for path tracking and lateral stability if it is adopted [13].

The aim of this paper is to compare three types of coordinated controllers, PTC#1, PTC#2, and PTC#3, for PTC and VSC on low-friction road conditions. As a state variable, e_y, e_φ, β, and γ are selected, and these variables are included in the LQ objective function for PTC and VSC. In the state-space model, a preview function is introduced. In PTC#1, four input configurations, $[\delta_f]$, $[\delta_f\ \delta_r]$, $[\delta_f\ \Delta M_z]$ and $[\delta_f\ \delta_r\ \Delta M_z]$, are selected from three control inputs, δ_f, δ_r, and ΔM_z. If ΔM_z is selected as a control input, a control allocation method is adopted to distribute it to the tire forces generated using multiple actuators. As an actuator for control allocation, 4WID and 4WIB are adopted [13,39]. To compare those controllers, a simulation is conducted using the vehicle simulation package, CarSim. The double lane change maneuver for collision avoidance is adopted as a test scenario [11,12,20,26,27,37]. From the simulation results, it is shown that there are few differences among the three types of coordinated controllers on low-friction roads.

The contributions of this paper can be condensed as follows:

1. This paper compares three types of coordinated controllers for PTC and VSC using LQR with regard to path-tracking performance. Different from the previous works, β and γ are included as state variables instead of the rates of lateral offset and heading errors. A preview function is also introduced into the state-space model. With the state vector, it is easier to include the preview function in the state-space model.

2. Through comparison, the effects of input configurations and controller structures on path-tracking performance under low-friction conditions were investigated. With the investigation, which type of controller is more effective than others for path tracking is determined.
3. From the comparison results, the best control structure and input configuration for path tracking and vehicle stability on low-friction roads is recommended. If there are little differences among those types of controllers, the simplest one is the best.

This paper consists of five sections. A design procedure of three types of coordinated controllers is described in Section 2. In Section 3, several measures for path-tracking performance are presented. The simulation is carried out and the simulation results are discussed in terms of the performance measures in Section 4. The conclusion is provided in Section 5.

2. Design of Controllers for Coordinated Control of Path Tracking and Vehicle Stability

2.1. Derivation of State-Space Model

Following the literature of PTC, a 2-DOF bicycle model is selected as vehicle one. Figure 2 shows the coordinates and variables of the bicycle model and the target path used for path tracking [12,13]. This model describes the lateral and yaw motions of a vehicle under the assumption that v_x is constant. With γ and β as a state variable, the equations of motions for the model are obtained as (1) [42,43]. At the front and rear wheels, the slip angles, α_f and α_r, are defined as (2) under the assumption that $\tan^{-1}(\theta) \approx \theta$ for small θ. The lateral tire forces, F_{yf} and F_{yr}, at the front and rear wheels are calculated as (3) under the assumption that the lateral tire force is linear with respect to the slip angle. By combining (1), (2), and (3), the linear state-space equations for the bicycle model are derived as (4).

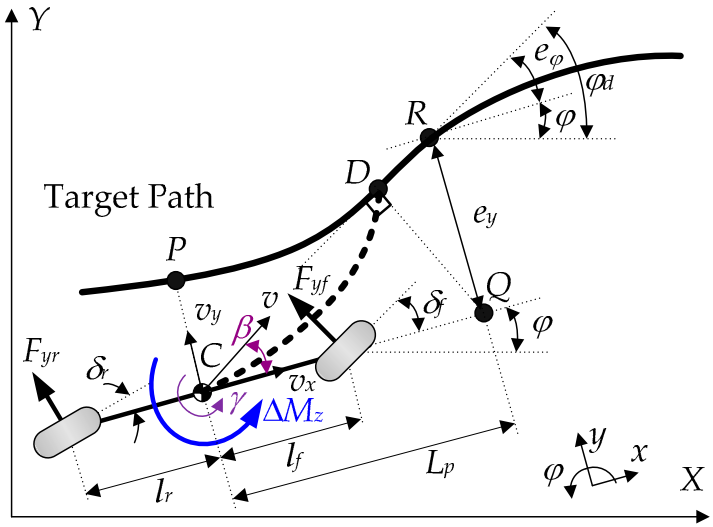

Figure 2. Coordinates and variables of the 2-DOF bicycle model and the target path.

$$\begin{cases} mv_x\left(\dot{\beta}+\gamma\right) = F_{yf}+F_{yr} \\ I_z\dot{\gamma} = l_fF_{yf}-l_rF_{yr}+\Delta M_z \end{cases} \tag{1}$$

$$\begin{cases} \alpha_f = \delta_f - \tan^{-1}\left(\beta+\frac{l_f\gamma}{v_x}\right) \approx \delta_f-\beta-\frac{l_f\gamma}{v_x} \\ \alpha_r = \delta_r - \tan^{-1}\left(\beta-\frac{l_r\gamma}{v_x}\right) \approx \delta_r-\beta+\frac{l_r\gamma}{v_x} \end{cases} \tag{2}$$

$$F_{yf} = 2C_f\alpha_f,\ F_{yr} = 2C_r\alpha_r \tag{3}$$

$$\begin{aligned}
\dot{\beta} &= \left(\frac{\varsigma_1}{mv_x}\right)\beta + \left(\frac{\varsigma_2}{mv_x^2} - 1\right)\gamma + \frac{C_f}{mv_x}\delta_f + \frac{C_f}{mv_x}\delta_r \\
\dot{\gamma} &= \left(\frac{\varsigma_2}{I_z}\right)\beta + \left(\frac{\varsigma_3}{I_z v_x}\right)\gamma + \frac{l_f C_f}{I_z}\delta_f - \frac{l_r C_r}{I_z}\delta_r + \frac{\Delta M_z}{I_z} \\
\varsigma_1 &= -C_f - C_r,\ \varsigma_2 = -C_f l_f + C_r l_r,\ \varsigma_3 = -l_f^2 C_f - l_r^2 C_r
\end{aligned} \tag{4}$$

In the literature of PTC, the lateral offset and heading errors, e_y and e_φ, have been defined at point P in Figure 2. In this paper, a lookahead or preview function is introduced to improve the path-tracking performance when calculating those errors [12,21,22,24,34,38,40]. The lookahead or preview distance L_p is calculated using (5). In (5), t_p is the preview interval or preview time, which acts as a velocity gain. In Figure 2, point C is located at the center of gravity (C.G.) of a vehicle. With L_p, the lookahead point Q and the point R on the target path are obtained. At point R, the time-derivative of e_y and e_φ is calculated as (6) under the assumption that e_φ is smaller than 10° and its consequence is $\sin e_\varphi \approx e_\varphi$.

$$L_p = t_p \cdot v_x \tag{5}$$

$$\begin{cases} \dot{e}_y = v_x \sin e_\varphi - v_x\beta - L_p\gamma \approx v_x e_\varphi - v_x\beta - L_p\gamma \\ \dot{e}_\varphi = \dot{\varphi}_d - \dot{\varphi} = v_x\chi - \gamma \end{cases} \tag{6}$$

With the state variables of e_y, e_φ, β, and γ, the state vector, $\mathbf{x}$, the disturbance, $\mathbf{w}$, and the control input, $\mathbf{u}$, are defined as (7). From (4), (6), and (7), the state-space equation for PTC and VSC is obtained as (8) [21,22,24]. In (8), the system, disturbance, and input matrices, $\mathbf{A}$, $\mathbf{B}_1$, and $\mathbf{B}_2$, are defined in (9).

$$\mathbf{x} = \begin{bmatrix} e_y & e_\varphi & \beta & \gamma \end{bmatrix}^T,\ \mathbf{w} = \chi,\ \mathbf{u} = \begin{bmatrix} \delta_f & \delta_r & \Delta M_z \end{bmatrix}^T \tag{7}$$

$$\dot{\mathbf{x}} = \mathbf{A}\mathbf{x} + \mathbf{B}_1\mathbf{w} + \mathbf{B}_{2\mathbf{u}} \tag{8}$$

$$\mathbf{A} = \begin{bmatrix} 0 & v_x & -v_x & -L_p \\ 0 & 0 & 0 & -1 \\ 0 & 0 & \frac{\varsigma_1}{mv_x} & \frac{\varsigma_2}{mv_x^2} - 1 \\ 0 & 0 & \frac{\varsigma_2}{I_z} & \frac{\varsigma_3}{I_z v_x} \end{bmatrix},\ \mathbf{B}_1 = \begin{bmatrix} 0 \\ v_x \\ 0 \\ 0 \end{bmatrix},\ \mathbf{B}_2 = \begin{bmatrix} 0 & 0 & 0 \\ 0 & 0 & 0 \\ \frac{C_f}{mv_x} & \frac{C_r}{mv_x} & 0 \\ \frac{l_f C_f}{I_z} & -\frac{l_r C_r}{I_z} & \frac{1}{I_z} \end{bmatrix} \tag{9}$$

The control input $\mathbf{u}$ defined in (7) is composed of δ_f, δ_r, and ΔM_z. From those elements of the control input $\mathbf{u}$, four control inputs, $\mathbf{u}_1$, $\mathbf{u}_2$, $\mathbf{u}_3$, and $\mathbf{u}_4$, are set as (10), which correspond to the input configurations, *IC*#1, *IC*#2, *IC*#3, and *IC*#4, respectively [13]. According to four control inputs, $\mathbf{u}_1$, $\mathbf{u}_2$, $\mathbf{u}_3$, and $\mathbf{u}_4$, the input matrices, $\mathbf{B}_{21}$, $\mathbf{B}_{22}$, $\mathbf{B}_{23}$, and $\mathbf{B}_{24}$, are defined in (10) from (9) [13]. In (10), $\mathbf{B}_2(k)$ represents the k-th column of the matrix $\mathbf{B}_2$ in (9). As shown in (10), δ_f is available for all ICs. δ_r is available for *IC*#2, *IC*#3, and *IC*#4. For *IC*#3 and *IC*#4 with ΔM_z, 4WIB and 4WID are available when generating ΔM_z. ΔM_z in *IC*#3 and *IC*#4 should be converted into δ_r and the braking and traction torques (T_{Bi} and T_{Di}) at each wheel using a control allocation procedure. For *IC*#4, RWS, i.e., δ_r, is not used when converting ΔM_z into tire forces because it is already included in the control input, $\mathbf{u}_4$. In this paper, it is assumed that T_{Bi} and T_{Di} are generated via 4WIB and 4WID, respectively. In this paper, *IC*#1 and *IC*#2 are used as a baseline of PTC#1. Moreover, *IC*#1 is used as a steering angle generator for PTC#2.

$$\begin{cases} \mathbf{u}_1 = \delta_f & \mathbf{B}_{21} = [\mathbf{B}_2(1)] & \text{for } IC\#1 \\ \mathbf{u}_2 = \begin{bmatrix} \delta_f & \delta_r \end{bmatrix}^T & \mathbf{B}_{22} = \begin{bmatrix} \mathbf{B}_2(1) & \mathbf{B}_2(2) \end{bmatrix} & \text{for } IC\#2 \\ \mathbf{u}_3 = \begin{bmatrix} \delta_f & \Delta M_z \end{bmatrix}^T & \mathbf{B}_{23} = \begin{bmatrix} \mathbf{B}_2(1) & \mathbf{B}_2(3) \end{bmatrix} & \text{for } IC\#3 \\ \mathbf{u}_4 = \begin{bmatrix} \delta_f & \delta_r & \Delta M_z \end{bmatrix}^T & \mathbf{B}_{24} = \begin{bmatrix} \mathbf{B}_2(1) & \mathbf{B}_2(2) & \mathbf{B}_2(3) \end{bmatrix} & \text{for } IC\#4 \end{cases} \tag{10}$$

2.2. Design of LQR for PTC#1 and PTC#2

LQ objective functions, J_1, J_2, J_3, and J_4, for input configurations, *IC*#1, *IC*#2, *IC*#3, and *IC*#4, of (10) are provided in (11), respectively. As shown in (11), the first two terms of J_0 including e_y and e_φ represent the path-tracking objective, and the last two terms of J_0 including β and γ represent the vehicle stability objective, which can be divided into lateral stability and yaw rate tracking. In this manner, PTC and VSC are integrated into a single control framework. J_1, J_2, J_3, and J_4 can be converted into the vector matrix form of (12). In (12), the matrices $\mathbf{Q}$ and $\mathbf{R}_i$ are provided as (13). In (11) and (13), the weight ρ_i is set using Bryson's rule, (14), where ξ_i is the maximum allowable value of the corresponding term [44]. The actual tuning procedure for path tracking and vehicle stability is carried out by adjusting ξ_i. The control input $\mathbf{u}_i$ of *IC*#*i* in LQR is calculated as (15), where $\mathbf{S}_i$ is the solution of the Riccati equation for *IC*#*i*.

$$J_0 = \int_0^\infty \left\{\rho_1 e_y^2 + \rho_2 e_\varphi^2 + \rho_3 \beta^2 + \rho_4 \gamma^2\right\} dt$$

$$\begin{cases} J_1 = J_0 + \int_0^\infty \left(\rho_5 \delta_f^2\right) dt & \text{for } IC\#1 \\ J_2 = J_0 + \int_0^\infty \left(\rho_5 \delta_f^2 + \rho_6 \delta_r^2\right) dt & \text{for } IC\#2 \\ J_3 = J_0 + \int_0^\infty \left(\rho_5 \delta_f^2 + \rho_7 \Delta M_z^2\right) dt & \text{for } IC\#3 \\ J_4 = J_0 + \int_0^\infty \left(\rho_5 \delta_f^2 + \rho_6 \delta_r^2 + \rho_7 \Delta M_z^2\right) dt & \text{for } IC\#4 \end{cases} \tag{11}$$

$$J_i == \int_0^\infty \begin{bmatrix} \mathbf{x} \\ \mathbf{u}_i \end{bmatrix}^T \begin{bmatrix} \mathbf{Q} & \mathbf{0} \\ \mathbf{0} & \mathbf{R}_i \end{bmatrix} \begin{bmatrix} \mathbf{x} \\ \mathbf{u}_i \end{bmatrix} dt,\ i = 1, \cdots, 4 \tag{12}$$

$$\mathbf{Q} = diag(\rho_1, \rho_2, \rho_3, \rho_4),\ \begin{cases} \mathbf{R}_1 = \rho_5 & \text{for } IC\#1 \\ \mathbf{R}_2 = diag(\rho_5, \rho_6) & \text{for } IC\#2 \\ \mathbf{R}_3 = diag(\rho_5, \rho_7) & \text{for } IC\#3 \\ \mathbf{R}_4 = diag(\rho_5, \rho_6, \rho_7) & \text{for } IC\#4 \end{cases} \tag{13}$$

$$\rho_i = \frac{1}{\xi_i^2} \tag{14}$$

$$\mathbf{u}_i = \mathbf{K}_i \mathbf{x} = -\mathbf{R}_i^{-1} \mathbf{B}_{2i}^T \mathbf{S}_i \mathbf{x},\ i = 1, \cdots, 4 \tag{15}$$

2.3. Derivation of the Reference Yaw Rate for PTC#2 and PTC#3

There are two methods that have been used to derive the reference yaw rate, γ_{ref}. The first method uses the FWS angle and the bicycle model provided in (4), and the second is to use a target path. In the first method, γ_{ref} is calculated to γ_s as provided in (16) [12,18,19,31–33,35–37,42]. The front steering angle, δ_f, is obtained from the LQR with *IC*#1 of PTC#1. In (16), K_γ is the steady-state yaw rate gain. In the previous study, it was shown that K_γ can be tuned regardless of C_f, C_r, m, and v_x for the purpose of enhancing path-tracking performance [11]. Generally, γ_s is bounded by (17) [43].

$$\gamma_s = \frac{2 \cdot C_f \cdot C_r \cdot \left(l_f + l_r\right) \cdot v_x}{2 \cdot C_f \cdot C_r \cdot \left(l_f + l_r\right)^2 + m \cdot v_x^2 \cdot \left(l_r \cdot C_r - l_f \cdot C_f\right)} \cdot \delta_f = K_\gamma \cdot \delta_f \tag{16}$$

$$\gamma_s \leq 0.85 \frac{\mu g}{v_x} \tag{17}$$

In the second method, γ_{ref} is obtained from a target path without a vehicle model [11,38–40]. The typical method for this purpose is to derive γ_p from Figure 1 as provided in (18) [38]. Another method is to use a polynomial interpolation, which is

adopted in this paper [11,12,39]. Figure 1 shows the desired and target paths and three points, *C*, *D*, and *Q*. Let the coordinate values of the points, *C*, *D*, and *Q*, be (x_0,y_0), (x_1,y_1), and (x_2,y_2), respectively. In Figure 1, the desired path is marked as a dashed bold line, connecting points *C* and *D*. To derive γ_{ref} for PTC, the curvature of the desired path should be calculated. Under the assumption that point *D* is close enough to the vehicle, the desired path is represented with a second-order polynomial, as provided in (19). Three coefficients, a_1, a_2, and a_3, of the polynomial are determined using (20) from the positions of the points *C* and *D* and the slope at the point *C*. With the coefficients of the polynomial, the curvature χ_d at point *C* is calculated as in (21). Finally, γ_{ref} for PTC is calculated into γ_d as in (22) [11,39]. In (22), the preview interval K_p plays an identical role to K_γ in (16). In this paper, K_p is set to 1 and γ_d is also limited by (17).

$$\gamma_p = \frac{2}{t_p}\left\{\tan^{-1}\left(\frac{e_y}{L_p}\right) - \beta\right\} \tag{18}$$

$$y(x) = a_1 x^2 + a_2 x + a_3 \tag{19}$$

$$\begin{bmatrix} a_1 \\ a_2 \\ a_3 \end{bmatrix} = \begin{bmatrix} {x_0}^2 & x_0 & 1 \\ {x_1}^2 & x_1 & 1 \\ 2x_0 & 1 & 0 \end{bmatrix}^{-1} \begin{bmatrix} y_0 \\ y_1 \\ y'(x_0) \end{bmatrix} \tag{20}$$

$$\chi_d = \frac{y''(x_0)}{\left\{1 + y'(x_0)^2\right\}^{3/2}} = \frac{2a_1}{\left\{1 + (2a_1 x_0 + a_2)^2\right\}^{3/2}} \tag{21}$$

$$\gamma_d = K_p \cdot v_x \cdot \chi_d \tag{22}$$

2.4. Design of Yaw Rate Tracking Controller for PTC#2 and PTC#3

To make γ follow the reference yaw rates, γ_s or γ_d, it is necessary to calculate ΔM_z. The yaw rate error, γ_e, is defined as (23), where this is set to the error surface, *s*. To make the surface asymptotically converge to zero, the condition of (24) should be satisfied [11,12,18,19,39]. By combining (1), (23), and (24), ΔM_z is computed as (25). In this paper, K_c is set to 5.

$$s = \gamma_e = \gamma - \gamma_{ref} \tag{23}$$

$$\dot{s} = -K_c s \ (K_c > 0) \tag{24}$$

$$\Delta M_z = I_z \cdot \dot{\gamma}_d - l_f F_{yf} + l_r F_{yr} - I_z \cdot K_c \cdot \left(\gamma - \gamma_{ref}\right) \tag{25}$$

2.5. Control Allocation with WLS for PTC#1, PTC#2, and PTC#3

The control yaw moment, ΔM_z, is obtained commonly from PTC#1, PTC#2, and PTC#3. Once ΔM_z is obtained, it should be converted into the longitudinal of wheels, which are generated using the actuators, i.e., 4WIB and 4WID, via a control allocation. For control allocation, a weighted least square (WLS)-based method is adopted in this paper [20–37].

Figure 3 shows tire forces at each wheel and ΔM_z, when ΔM_z is positive [13,18,19,45]. In Figure 3, ΔF_{yf} and ΔF_{yr} are the lateral tire forces of the front and rear wheels, which are generated via FWS and RWS, respectively. ΔF_{x1}, ΔF_{x2}, ΔF_{x3}, and ΔF_{x4} are the longitudinal tire forces generated via 4WID and 4WIB. If ΔF_i is positive, it is generated as the traction torque T_{Di} via 4WID. Otherwise, it is generated as the braking torque T_{Bi} via 4WIB. These six tire forces should be determined to generate ΔM_z. The WLS-based method is used for this purpose.

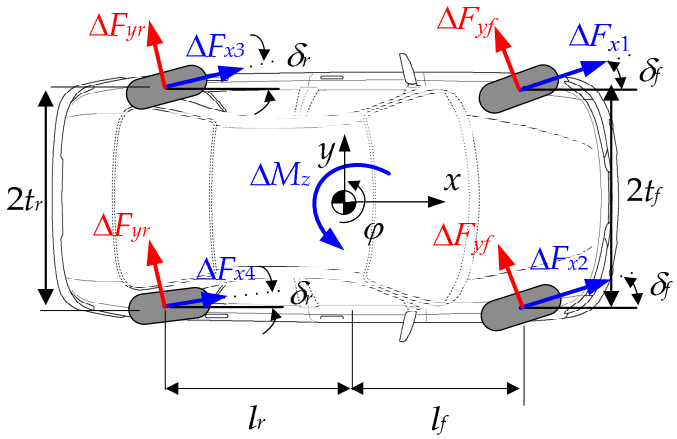

Figure 3. Coordinate system on vehicle geometry with tire forces and yaw moment control.

From the geometric relationship shown in Figure 3, the equilibrium condition among ΔM_z and tire forces is obtained as (26) [11,12,18,19,39]. In (26), the elements of the vector $\mathbf{p}$ are provided in (27).

$$\underbrace{\begin{bmatrix} p_1 & p_2 & p_3 & p_4 & p_5 & p_6 \end{bmatrix}}_{\mathbf{p}} \underbrace{\begin{bmatrix} \Delta F_{yf} \\ \Delta F_{yr} \\ \Delta F_{x1} \\ \Delta F_{x2} \\ \Delta F_{x3} \\ \Delta F_{x4} \end{bmatrix}}_{\mathbf{q}} = \Delta M_z \tag{26}$$

$$\begin{cases} p_1 = -2l_f \cos\delta_f,\ p_2 = 2l_r \cos\delta_r, \\ p_3 = -l_f \sin\delta_f + t_f \cos\delta_f,\ p_4 = -l_f \sin\delta_f - t_f \cos\delta_f, \\ p_5 = l_r \sin\delta_r + t_r \cos\delta_r,\ \ p_6 = l_r \sin\delta_r - t_r \cos\delta_r \end{cases} \tag{27}$$

The objective function of WLS is defined with the quadratic form as in (28). In (28), μF_{zi} represents the radius of the friction circle at the wheel i. Assuming that the road surface is flat, it can be easily estimated using acceleration signals measured by sensors [46]. In (28), $\boldsymbol{\kappa}$ is the vector of virtual weights, κ_i, which is used to select the combination of actuators [39,47,48]. The equality constraint (26) is converted into the quadratic form (29). In the previous study, (26) must be satisfied in order to generate ΔM_z. The objective function (28) and the constraint (29) are combined into a single objective one (30), with the Lagrange multiplier, ζ. In (30), ζ should be set to 1 or higher. In this paper, ζ is set to 10. Otherwise, the constraint (26) is not satisfied. The optimum of (30) is algebraically obtained as (31) by differentiating (30) with respect to $\mathbf{q}$ [13].

$$\begin{aligned} J_E &= \frac{\kappa_1 \Delta F_{yf}^2 + \kappa_3 \Delta F_{x1}^2}{(\mu F_{z1})^2} + \frac{\kappa_1 \Delta F_{yf}^2 + \kappa_4 \Delta F_{x2}^2}{(\mu F_{z2})^2} + \frac{\kappa_2 \Delta F_{yf}^2 + \kappa_5 \Delta F_{x3}^2}{(\mu F_{z3})^2} + \frac{\kappa_2 \Delta F_{yf}^2 + \kappa_6 \Delta F_{x4}^2}{(\mu F_{z4})^2} = \mathbf{p}^T \mathbf{W} \mathbf{p} \\ \mathbf{W} &= \mathrm{diag}\left[\frac{1}{(\mu F_{z1})^2} + \frac{1}{(\mu F_{z2})^2}, \frac{1}{(\mu F_{z3})^2} + \frac{1}{(\mu F_{z4})^2}, \frac{1}{(\mu F_{z1})^2}, \frac{1}{(\mu F_{z2})^2}, \frac{1}{(\mu F_{z3})^2}, \frac{1}{(\mu F_{z4})^2} \right] \boldsymbol{\kappa} \\ \boldsymbol{\kappa} &= \mathrm{diag}\begin{bmatrix} \kappa_1 & \kappa_2 & \kappa_3 & \kappa_4 & \kappa_5 & \kappa_6 \end{bmatrix} \end{aligned} \tag{28}$$

$$J_{EC} = (\mathbf{pq} - \Delta M_z)^T (\mathbf{pq} - \Delta M_z) \tag{29}$$

$$J_{CA} = J_E + \zeta \cdot J_{EC} = \mathbf{q}^T \mathbf{W} \mathbf{q} + \zeta (\mathbf{pq} - \Delta M_z)^T (\mathbf{pq} - \Delta M_z) \tag{30}$$

$$\mathbf{q}_{opt} = \zeta\left(\mathbf{W} + \eta\mathbf{p}^T\mathbf{p}\right)^{-1}\mathbf{p}^T\Delta M_z \tag{31}$$

When applying WLS for control allocation with ΔM_z, arbitrary actuator combinations composed of FWS, RWS, 4WS, 4WIB, and 4WID can be set according to a particular input configuration. For example, if $\mathbf{u}_4$ of *IC*#4 in (10) is selected as a control input, only 4WID and 4WIB are available to be used in generating ΔM_z because δ_f and δ_r of FWS, RWS, and 4WS are already determined using LQR. To reflect this fact, the virtual weights, κ_i, can be set according to a particular combination of multiple actuators, FWS, RWS, 4WS, 4WIB, and 4WID [39,47,48].

The vectors of virtual weights corresponding to steering actuators, i.e., FWS, RWS, and 4WS, are provided in (32). Initially, all the virtual weights are set to 1. In (32), ε is 10^{-4} and the terms denoted by $\bullet$ have no effect on the steering actuators. The first and second terms of $\boldsymbol{\kappa}$ in (32) correspond to ΔF_{yf} and ΔF_{yr}, respectively, which are converted into the front and rear steering angles. If the first term of $\boldsymbol{\kappa}$ is set to ε, then only ΔF_{yf} is generated via WLS. This is shown in the first row of (32).

$$\begin{cases} \text{FWS}: & \boldsymbol{\kappa} = \text{diag}\begin{bmatrix} \varepsilon & 1 & \bullet & \bullet & \bullet & \bullet \end{bmatrix} \\ \text{RWS}: & \boldsymbol{\kappa} = \text{diag}\begin{bmatrix} 1 & \varepsilon & \bullet & \bullet & \bullet & \bullet \end{bmatrix} \\ \text{4WS}: & \boldsymbol{\kappa} = \text{diag}\begin{bmatrix} \varepsilon & \varepsilon & \bullet & \bullet & \bullet & \bullet \end{bmatrix} \end{cases} \tag{32}$$

The vectors of virtual weights representing 4WIB and 4WID are provided in (33). Figure 3 shows the fact that only ΔF_{x2} and ΔF_{x4} should be generated if ΔM_z is negative and 4WIB is available. This is represented by the second row of the first term, 4WIB in (33). If 4WIB and 4WID are available for generating ΔM_z, no constraints are imposed on the longitudinal forces, which is represented by the last row of (33), i.e., 4WID + 4WIB. The virtual weights provided in (32) and (33) can be set according to combinations of actuators available for the purpose of generating ΔM_z.

$$\begin{cases} \text{4WID}: & \begin{cases} \boldsymbol{\kappa} = \text{diag}\begin{bmatrix} \bullet & \bullet & 1 & \varepsilon & 1 & \varepsilon \end{bmatrix} \text{ if } \Delta M_z > 0 \\ \boldsymbol{\kappa} = \text{diag}\begin{bmatrix} \bullet & \bullet & \varepsilon & 1 & \varepsilon & 1 \end{bmatrix} \text{ if } \Delta M_z < 0 \end{cases} \\ \text{4WIB}: & \begin{cases} \boldsymbol{\kappa} = \text{diag}\begin{bmatrix} \bullet & \bullet & \varepsilon & 1 & \varepsilon & 1 \end{bmatrix} \text{ if } \Delta M_z > 0 \\ \boldsymbol{\kappa} = \text{diag}\begin{bmatrix} \bullet & \bullet & 1 & \varepsilon & 1 & \varepsilon \end{bmatrix} \text{ if } \Delta M_z < 0 \end{cases} \\ \text{4WID} + \text{4WIB}: & \boldsymbol{\kappa} = \text{diag}\begin{bmatrix} \bullet & \bullet & \varepsilon & \varepsilon & \varepsilon & \varepsilon \end{bmatrix} \end{cases} \tag{33}$$

In this paper, T_{Bi} and T_{Di} at the wheel i are calculated from ΔF_{x1}, ΔF_{x2}, ΔF_{x3}, and ΔF_{x4}, determined via the WLS-based method, i.e., $\mathbf{q}_{opt}$ in (31). Following the sign of ΔF_{xi}, $T_{Bi,}$ and T_{Di} at the wheel i are calculated as (34), respectively [13].

$$\begin{Bmatrix} T_{Bi} & \text{if } \Delta F_{xi} < 0 \\ T_{Di} & \text{if } \Delta F_{xi} > 0 \end{Bmatrix} = h\left(\frac{r_{wi}\Delta F_{xi}}{v_i}, \omega_i\right), \quad i = 1, \cdots, 4 \tag{34}$$

δ_f and δ_r are calculated from ΔF_{yf} and ΔF_{yr} obtained in $\mathbf{q}_{opt}$ and the definitions of (2) and (3). The definition of the lateral tire force (3) is rewritten as (35). In (35), σ is the parameter representing the magnitude of the cornering stiffness, C_i [34]. In this paper, σ is set to 6. For 4WS, δ_f and δ_r are calculated as (36) by combining (2) with (35) [13,49]. In these formulations, β is needed. However, it is hard to measure. For this reason, an extended Kalman Filter is adopted to estimate β [50] in this paper.

$$\phi_i = -\frac{\Delta F_{yi}}{\sigma C_i}, \; i = f, r \tag{35}$$

$$\begin{cases} \delta_f = -\alpha_f + \beta + \frac{l_f\gamma}{v_x} = -\phi_f + \beta + \frac{l_f\gamma}{v_x} \\ \delta_r = -\alpha_r + \beta - \frac{l_r\gamma}{v_x} = -\phi_r + \beta - \frac{l_r\gamma}{v_x} \end{cases} \tag{36}$$

3. Performance Measures for Path Tracking and Vehicle Stability

In the literature of PTC, e_y and e_φ have been used to represent the path-tracking performance. Different from the literature on PTC, a double lane change maneuver for collision avoidance is adopted as a target path in this paper [11–13,20,26,27,37]. This path has been used to measure the reachability and agility of a path-tracking controller [12,13]. Figure 4 shows the target path and vehicle trajectory. From the points on the target path and the vehicle trajectory in Figure 4, five measures standing for path-tracking performance are defined as (37): the peak's center offset, ΔX, the peak's lateral offset, ΔY, the percentage over-shoot, $OS\%$, the response delay, ΔDX, and the settling delay, ΔSX. These measures are illustrated in Figure 4. In (37), the subscripts X and Y represent the x- and y-positions of the point •, respectively. Basically, the smaller the absolute magnitudes of these measures, the better the path-tracking performance.

$$\begin{cases} \Delta X = D_X - A_X = D_X - 73.20 \\ \Delta Y = D_Y - A_Y = D_Y - 3.53 \\ \Delta DX = E_X - B_X = E_X - 91.50 \\ \Delta SX = G_X - C_X = G_X - 190.00 \\ OS\% = \dfrac{|F_Y| - 1.65}{1.65 + 3.53} \times 100 \end{cases} \tag{37}$$

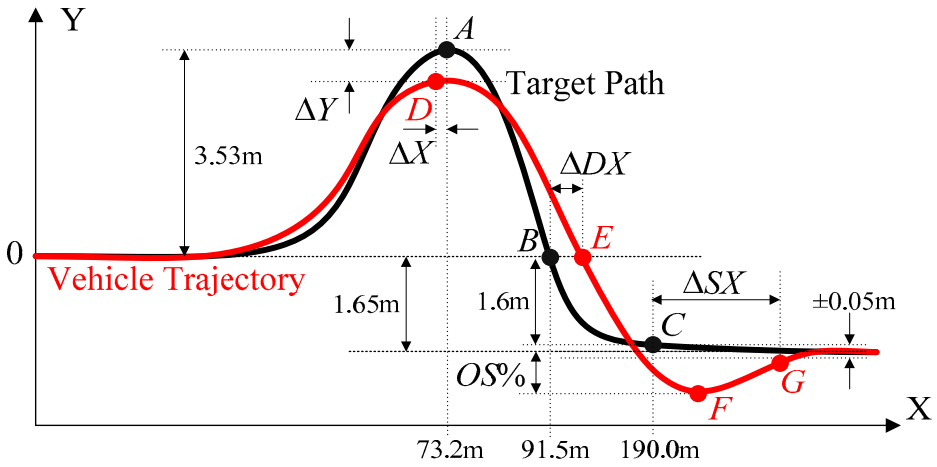

Figure 4. Measures for path-tracking performance.

In Figure 4, ΔX and ΔY represent the agility and the reachability, respectively. In this paper, if ΔY is larger than -0.05 m, it is regarded that the path-tracking performance of a controller is satisfactory. $OS\%$ stands for lateral damping, which represents agility. In this paper, it is satisfactory if $OS\%$ is less than 16%, which is equal to the overshoot of 0.85 m. ΔDX stands for the response delay, which stands for the agility of the longitudinal motion. ΔSX can be regarded as the settling time, which stands for the convergence speed of the vehicle's lateral motion to a target value of y-position. In this paper, it is satisfactory if ΔSX is less than 16 m. Generally, if $OS\%$ is near 1% under the condition that ΔY is larger than -0.05 m, the best performance is achieved. Detailed explanations of these measures can be found in [12,13].

As mentioned earlier, VSC stands for yaw rate tracking and lateral stability. Generally, yaw rate tracking performance is measured with the yaw rate error γ_e and lateral stability performance is measured with β. It has been regarded that lateral stability performance is satisfactory if β is less than 3° [51]. Let us denote the maximum absolute value of β to be MASSA. The side-slip angular rate, combined with β, has been also used as a measure of lateral stability. Let us denote the maximum absolute value of the side-slip angular rate to be MASSAR [12].

4. Simulation and Discussion

4.1. Simulation Environment

A simulation was conducted to compare three controllers, PTC#1, PTC#2, and PTC#3, on low-friction roads in terms of path-tracking performance. These controllers were implemented using MATLAB/Simulink (2019a) and connected with the vehicle simulation software CarSim 8 [52]. The configuration of MATLAB/Simulink and CarSim is provided in Figure 1. In Figure 1, the autonomous electrical vehicles with FWS/4WS, 4WID, and 4WIB are replaced by CarSim, and the other parts are implemented with MATLAB/Simulink. A target path in Figure 4 was selected as a test scenario. In the simulation, the built-in F-segment sedan model provided in the CarSim software was selected [52]. From the model, the parameters of the bicycle model are provided in Table 1. In Table 1, the cornering stiffness, C_f and C_r, are obtained from simulation in CarSim by comparing β and γ of CarSim and the state-space model under a step steering maneuver. The steering actuators of FWS and 4WS were modeled as the first-order system with a time constant of 0.05. 4WIB and 4WID were modeled as the first-order system with a time constant of 0.1. The initial v_x and μ were set to 60 km/h and 0.4, respectively. The speed controller provided in CarSim was applied upon driving to maintain a constant speed, which means that K_γ is maintained as constant as possible.

Table 1. Parameter of 2-DOF bicycle model obtained from F-segment sedan in CarSim.

Parameter	Value	Parameter	Value
m_s	1823 kg	I_z	6286 kg·m^2
C_f	42,000 N/rad	C_r	62,000 N/rad
l_f	1.27 m	l_r	1.90 m
t_f	0.80 m	t_r	0.80 m

In real vehicles, the magnitude of ΔM_z is limited by the maximum tire forces and road surface friction. To reflect this fact, it is necessary to set a bound on ΔM_z. For this purpose, ΔM_z is limited to a certain value after calculating it using LQR. For example, *IC*#4 of PTC#1 can use the smallest ΔM_z among the input configurations because only the longitudinal tire forces are available for control allocation. A detailed description of how to select the limit of ΔM_z can be found in Reference [13].

The tuning was carried out by trial and error such that ΔY is larger than -0.05 m and *OS*% is near 0.9, which gives the smallest ΔDX and ΔSX. The most important tuning parameters are the velocity gain t_p, ζ_1 and ζ_2 in (14). If RWS is adopted, the weight on RWS, i.e., ζ_6 in (14), should be set to a small value such that β is smaller than 2.5°.

4.2. Simulation with PTC#1

The first simulation was carried out with PTC#1. For *IC*#1, *IC*#2, *IC*#3, and *IC*#4, several actuator combinations composed of RWS, 4WS, 4WID, and 4WIB were used for control allocation. The tuning parameters of PTC#1 are t_p and ζ_i as provided in (5) and (14), respectively. The simulation results of PTC#1 are summarized in Table 2. The velocity gains and weights of the LQ objective function are provided in Table 3. As shown in Table 2, there are few differences among the input configurations and actuator combinations in terms of path-tracking performance. A notable feature is that the use of RWS increases MASSA. This is caused by the fact that RWS steers the rear wheels along the identical direction to the front wheels. These results are identical to those of [13].

Table 2. Summary of the simulation results for *IC*#1, *IC*#2, *IC*#3, and *IC*#4 of PTC#1.

	Actuator Combinations	ΔX (m)	ΔY (m)	$OS\%$	ΔDX (m)	ΔSX (m)	MASSA (deg)	MASSAR (deg/s)
IC#1	FWS	1.57	0.002	1.0	8.98	4.84	0.58	13.13
IC#2	4WS	1.61	0.013	0.9	9.12	5.06	1.67	14.73
IC#3	FWS + 4WID	1.19	−0.035	0.9	8.91	4.64	0.59	13.34
	+4WIB	1.29	−0.024	1.0	8.80	4.63	0.59	0.59
	+4WID + 4WIB	1.30	−0.015	1.0	8.71	4.59	0.59	13.22
	FWS + RWS	1.25	−0.003	0.9	8.74	4.58	1.36	13.84
	+4WID	1.35	0.000	1.0	8.87	4.70	1.35	14.02
	+4WIB	1.59	0.000	1.0	9.17	5.01	1.15	13.11
	+4WID + 4WIB	1.60	0.004	0.9	9.13	4.99	1.13	13.30
IC#4	+4WID	1.45	−0.002	0.9	9.21	5.07	2.09	15.30
	+4WIB	1.48	0.004	1.0	9.10	5.04	2.08	15.08
	+4WID + 4WIB	1.49	0.010	0.9	9.04	5.02	1.96	15.07

Table 3. Velocity gains and weights of LQ objective function for *IC*#1, *IC*#2, *IC*#3, and *IC*#4 of PTC#1.

	Actuator Combinations	t_p	ζ_1	ζ_2	ζ_3	ζ_4	ζ_5	ζ_6	ζ_7
IC#1	FWS	0.60	0.5600	5.000	0.30	10.00	0.05	-	-
IC#2	4WS	0.60	0.5500	0.700	0.30	10.0	0.05	0.005	-
IC#3	FWS + 4WID	1.19	0.0518	0.005	0.10	0.10	0.03	-	50.0
	+4WIB	1.29	0.0532	0.005	0.10	0.10	0.03	-	50.0
	+4WID + 4WIB	1.30	0.0572	0.005	0.10	0.10	0.03	-	50.0
	FWS + RWS	1.25	0.0662	0.005	0.10	0.10	0.03	-	50.0
	+4WID	1.35	0.0644	0.005	0.10	0.10	0.03	-	50.0
	+4WIB	1.59	0.0585	0.005	0.10	0.10	0.03	-	50.0
	+4WID + 4WIB	1.60	0.0598	0.005	0.10	0.10	0.03	-	50.0
IC#4	+4WID	1.45	0.0566	0.005	0.10	0.10	0.03	0.001	50.0
	+4WIB	1.48	0.0569	0.005	0.10	0.10	0.03	0.001	50.0
	+4WID + 4WIB	1.49	0.0606	0.005	0.10	0.10	0.03	0.001	50.0

For *IC*#3, ΔM_z is added to *IC*#1, i.e., FWS. As shown in Table 2, the ΔX of *IC*#3 is reduced by adding ΔM_z to *IC*#1. Especially, RWS and 4WID have a large effect on the reduction in ΔX. Among them, 4WID is preferred to RWS because 4WID does not increase MASSA. On the contrary, *IC*#4 adds ΔM_z to *IC*#2, i.e., 4WS. As shown in Table 2, there are few effects of adding ΔM_z to *IC*#2 on path-tracking performance although ΔX is slightly decreased by adding ΔM_z. In Table 2, the actuator combinations with RWS in *IC*#3 are equivalent to those of *IC*#4. As shown in Table 2, the former is better than the latter in terms of path-tracking performance. This fact means that the control allocation with multiple actuators for 4WS is not effective. Instead, it is desirable to add ΔM_z to *IC*#1 and use control allocation with multiple actuators. Besides the increase in MASSA and the reduction in ΔX, there are few effects of adding ΔM_z to *IC*#1 or *IC*#2. Figures 5–7 show the trajectories and side-slip angles of every input configuration and actuator combination provided in Table 2. As shown in these figures, there are little differences among trajectories. On the contrary, only the side-slip angles are different from one another. From these results, it can be concluded that it is desirable to not use the multiple actuators needed to generate ΔM_z for path tracking.

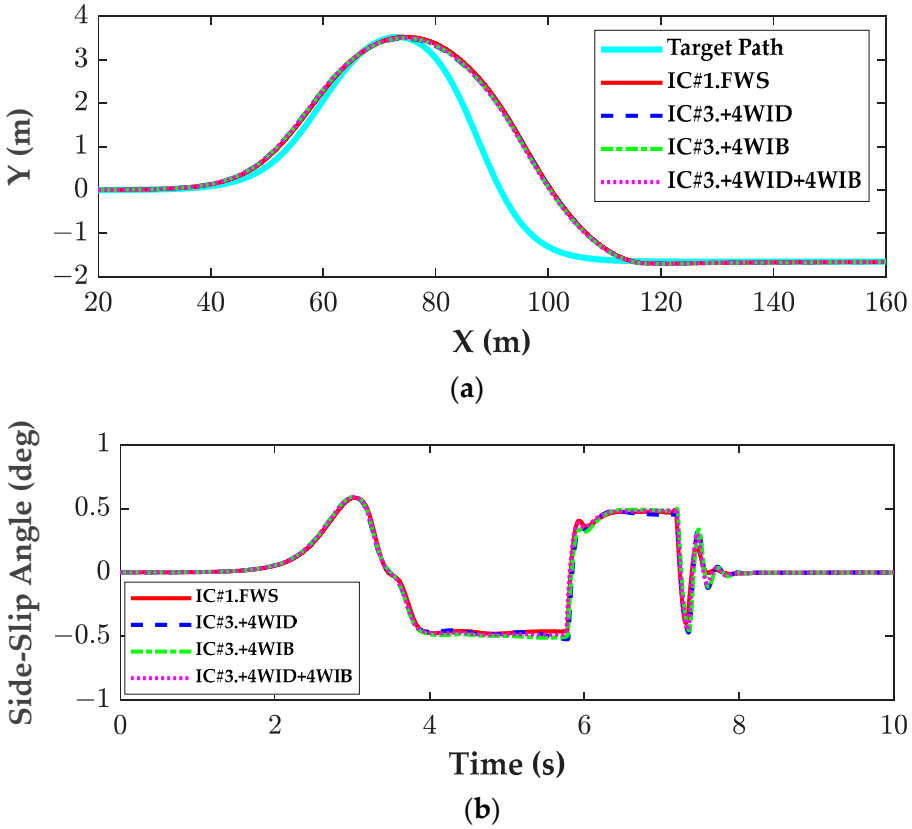

Figure 5. Simulation results with *IC*#1 and *IC*#3 of PTC#1. (**a**) Trajectories. (**b**) Side-slip angles.

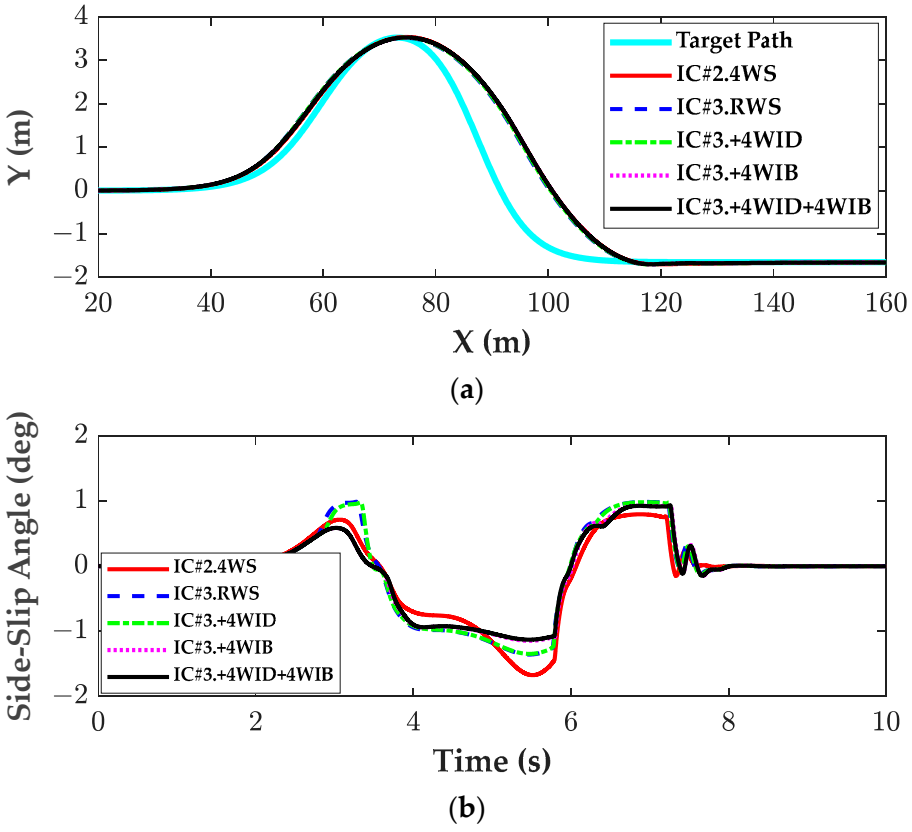

Figure 6. Simulation results with *IC*#2 and *IC*#3 of PTC#1. (**a**) Trajectories. (**b**) Side-slip angles.

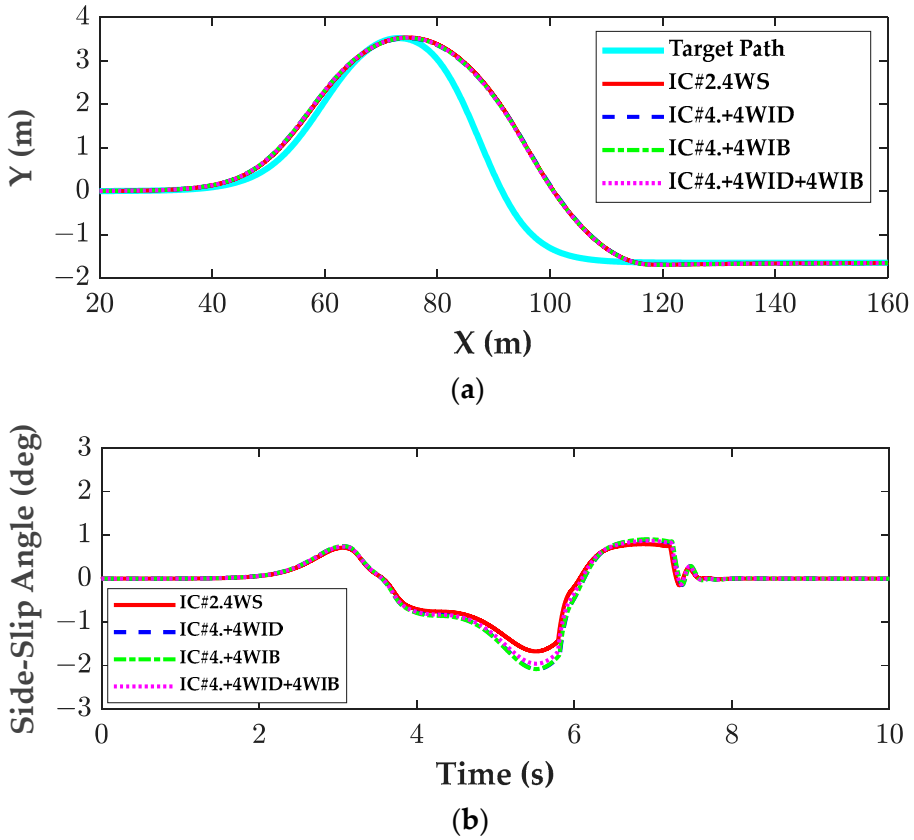

Figure 7. Simulation results with *IC*#2 and *IC*#4 of PTC#1. (**a**) Trajectories. (**b**) Side-slip angles.

4.3. Simulation with PTC#2 and PTC#3

The second simulation was carried out with PTC#2 and PTC#3. In PTC#2, the front steering angle needed to calculate the reference yaw rate is generated using the *IC*#1 of PTC#1. This is identical to PTC#3 except the reference yaw rate is calculated from a target path. With the reference yaw rate, ΔM_z is calculated using SMC. For this reason, RWS, 4WID, and 4WIB were used to generate ΔM_z in PTC#2 and PTC#3. Because PTC#2 and PTC#2 use the *IC*#1 of PTC#1 to generate δ_f, the tuning parameters of PTC#2 and PTC#3 are identical to those of PTC#1.

Tables 4 and 5 summarize the simulation results of PTC#2 and PTC#3, respectively. Table 6 shows the best and worst results for PTC#1, PTC#2, and PTC#3. In Table 5, *IC*#1 and *IC*#2 of PTC#1 are selected as a baseline, and the gray rows indicate the worst results. Tables 7 and 8 show the velocity gains and weights of LQ objective functions for PTC#2 and PTC#3, which correspond to Tables 4 and 5, respectively. Figures 8–11 show the trajectories and the side-slip angles of each actuator combination of PTC#2 and PTC#3, respectively. As shown in Table 4, the use of RWS increases MASSA, which is identical to PTC#1. Instead, ΔX is significantly reduced by RWS. As shown in Table 5, this tendency can also be identified via PTC#3. Without RWS, the 4WIB of PTC#2 provided the best result among PTC#1, PTC#2, and PTC#3. This fact can be identified in Figure 8. With RWS, the 4WID of PTC#2 provided a good result although MASSA was increased via RWS. By comparing the results among Tables 2, 4 and 6, it can be identified that PTC#2 is superior to PTC#1 in terms of path-tracking performance. By comparing PTC#1 and PTC#3 as shown in Tables 1, 5 and 6, PTC#1 and PTC#3 have no superiority over each other in terms of path-tracking performance.

Table 4. Summary of the simulation results for PTC#2.

Actuator Combinations	Δ*X* (m)	Δ*Y* (m)	*OS*%	Δ*DX* (m)	Δ*SX* (m)	MASSA (deg)	MASSAR (deg/s)
+4WID	1.50	−0.012	0.9	8.70	4.53	0.58	14.13
+4WIB	0.52	−0.036	0.9	6.66	2.40	0.66	12.56
+4WID + 4WIB	1.15	−0.028	1.0	8.89	5.39	0.64	13.39
+RWS	0.39	0.020	0.9	7.80	4.26	1.84	12.41
+4WID	0.42	0.026	0.9	7.66	3.88	1.67	12.39
+4WIB	0.68	0.023	0.9	8.02	4.24	1.54	12.08
+4WID + 4WIB	0.65	0.015	0.7	8.29	4.88	1.44	11.47

Table 5. Summary of the simulation results for PTC#3.

Actuator Combinations	Δ*X* (m)	Δ*Y* (m)	*OS*%	Δ*DX* (m)	Δ*SX* (m)	MASSA (deg)	MASSAR (deg/s)
+4WID	1.75	−0.033	1.0	9.07	4.76	0.68	13.59
+4WIB	1.56	−0.029	1.0	7.70	4.02	0.73	12.42
+4WID + 4WIB	1.67	−0.024	1.0	9.34	5.70	0.62	12.28
+RWS	1.08	−0.034	1.0	8.41	5.59	1.75	14.35
+4WID	0.93	−0.034	0.9	8.12	4.80	1.59	13.93
+4WIB	1.51	0.004	0.9	9.10	5.82	1.51	13.85
+4WID + 4WIB	1.01	−0.020	1.0	8.60	4.88	1.46	13.80

Table 6. Summary of the best results for PTC#1, PTC#2, and PTC#3.

PTC	Actuator Combinations	Δ*X* (m)	Δ*Y* (m)	*OS*%	Δ*DX* (m)	Δ*SX* (m)	MASSA (deg)	MASSAR (deg/s)
PTC#1	*IC*#1: FWS	1.57	0.002	1.0	8.98	4.84	0.58	13.13
	IC#2: RWS	1.61	0.013	0.9	9.12	5.06	1.67	14.73
	IC#3: FWS + RWS	1.25	−0.003	0.9	8.74	4.58	1.36	13.84
	IC#4: FWS + RWS + 4WID	1.45	−0.00	0.9	9.21	5.07	2.09	15.30
PTC#2	FWS + 4WIB	0.52	−0.036	0.9	6.66	2.40	0.66	12.56
	FWS + 4WID	1.5	−0.01	0.9	8.70	4.53	0.58	14.13
PTC#3	FWS + RWS + 4WID	0.93	−0.034	0.9	8.12	4.80	1.59	13.93
	FWS + RWS + 4WIB	1.51	0.004	0.9	9.10	5.82	1.51	13.85

Table 7. Velocity gains and weights of LQ objective functions for PTC#2.

Actuator Combinations	t_p	ζ_1	ζ_2	ζ_3	ζ_4	ζ_5
+4WID	0.065	0.0539	0.005	0.05	0.50	0.03
+4WIB	0.065	0.0740	0.005	0.05	0.50	0.03
+4WID + 4WIB	0.065	0.0626	0.005	0.05	0.50	0.03
+RWS	0.060	0.0700	0.005	0.10	0.50	0.03
+4WID	0.060	0.0818	0.005	0.10	0.50	0.03
+4WIB	0.060	0.0656	0.005	0.10	0.50	0.03
+4WID + 4WIB	0.060	0.0725	0.005	0.10	0.50	0.03

Table 8. Velocity gains and weights of LQ objective functions for PTC#3.

Actuator Combinations	t_p	ζ_1	ζ_2	ζ_3	ζ_4	ζ_5
+4WID	0.07	0.0734	0.010	0.05	0.50	0.03
+4WIB	0.07	0.1172	0.015	0.05	0.50	0.03
+4WID + 4WIB	0.07	0.1123	0.015	0.10	0.50	0.03
+RWS	0.07	0.0969	0.010	0.10	0.50	0.03
+4WID	0.07	0.1012	0.010	0.10	0.50	0.03
+4WIB	0.07	0.0935	0.010	0.10	0.50	0.03
+4WID + 4WIB	0.07	0.1045	0.010	0.10	0.50	0.03

Although PTC#2 provided better results than PTC#1, there are few differences among PTC#1, PTC#2, and PTC#3, as shown in the trajectories of Figures 5–11. The side-slip angles are less than 3° for all controllers, which is acceptable in terms of lateral stability. PTC#1 and PTC#3 require a two-level controller. Especially, *IC*#1 and *IC*#2 of PTC#1 do not require any control allocation schemes. On the contrary, PTC#2 requires a three-level controller including a yaw rate tracking controller and control allocation. As shown in Section 2, the yaw rate tracking controller and control allocation require several variables that are difficult to measure. For this reason, *IC*#1 and *IC*#2 of PTC#1 are the best choices for designing a path-tracking controller because they are the simplest among the controllers. Moreover, *IC*#1 of PTC#1 is preferred to *IC*#2 because it gives a smaller side-slip angle than *IC*#2.

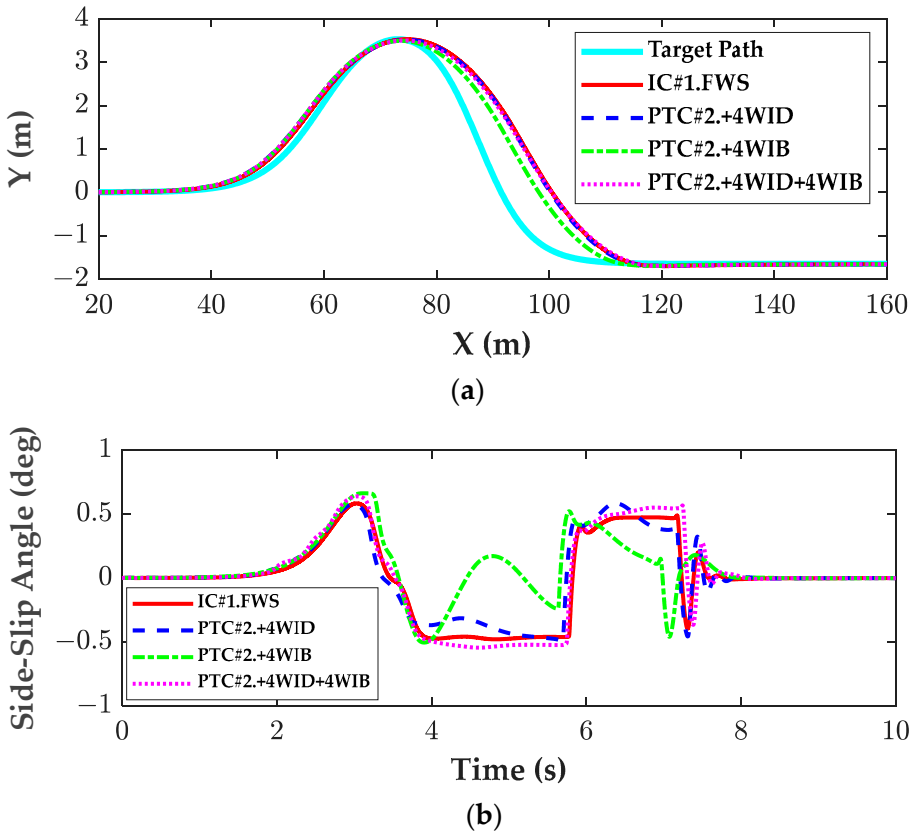

Figure 8. Simulation results with *IC*#1 and PTC#2. (**a**) Trajectories. (**b**) Side-slip angles.

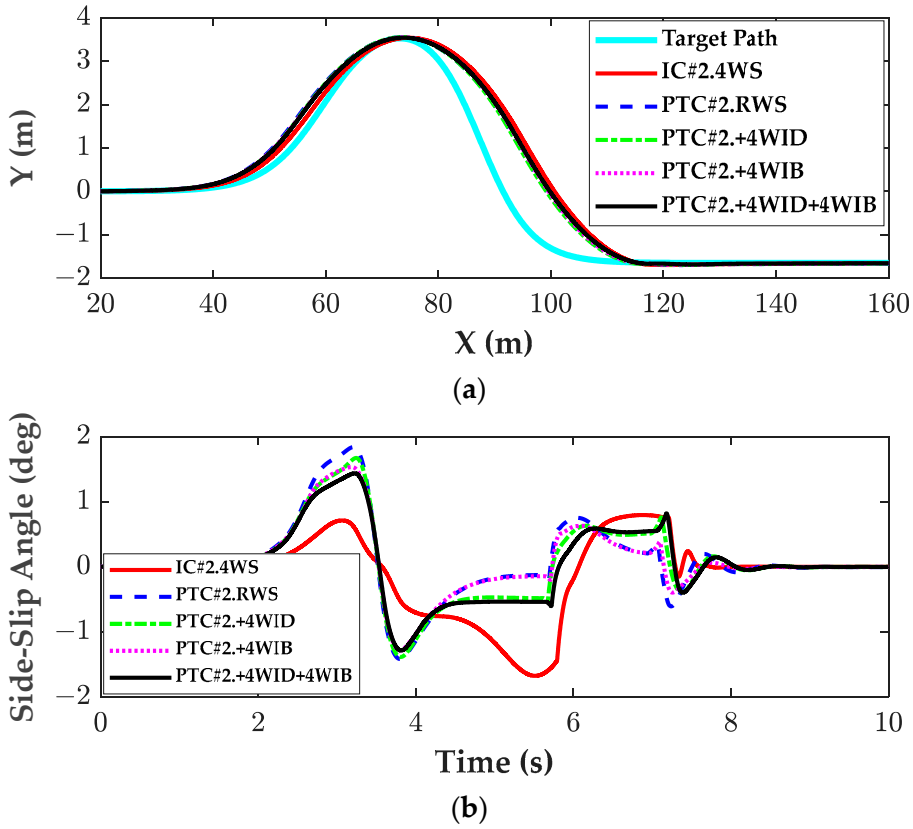

Figure 9. Simulation results with *IC*#2 and PTC#2. (**a**) Trajectories. (**b**) Side-slip angles.

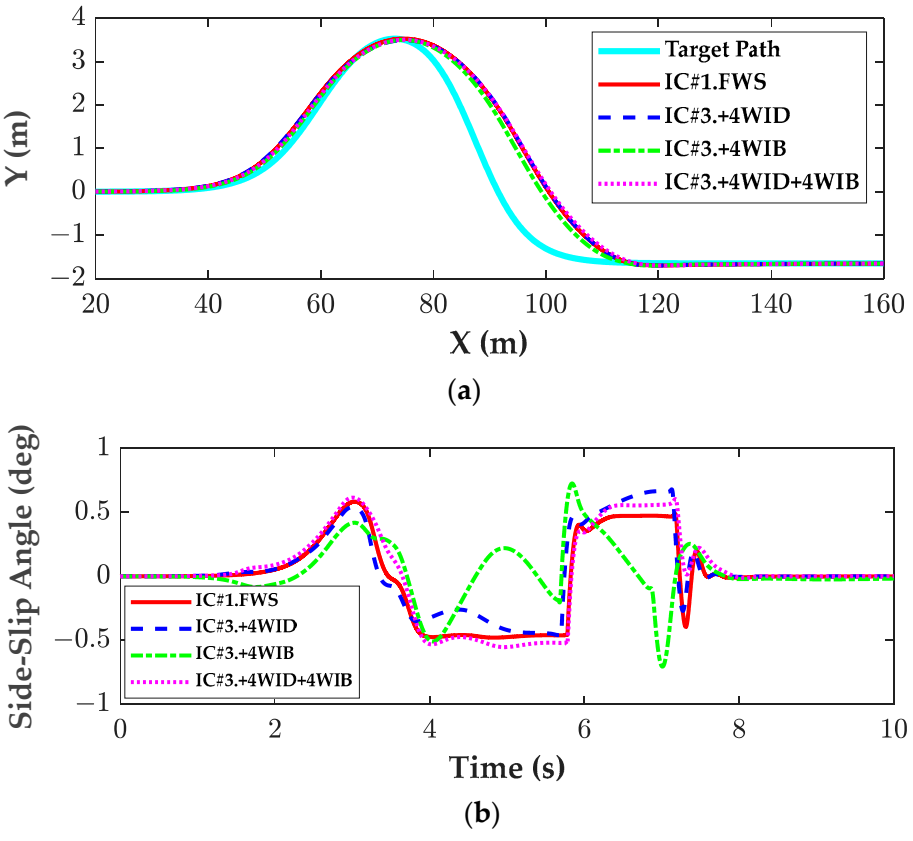

Figure 10. Simulation results with *IC*#1 and PTC#3. (**a**) Trajectories. (**b**) Side-slip angles.

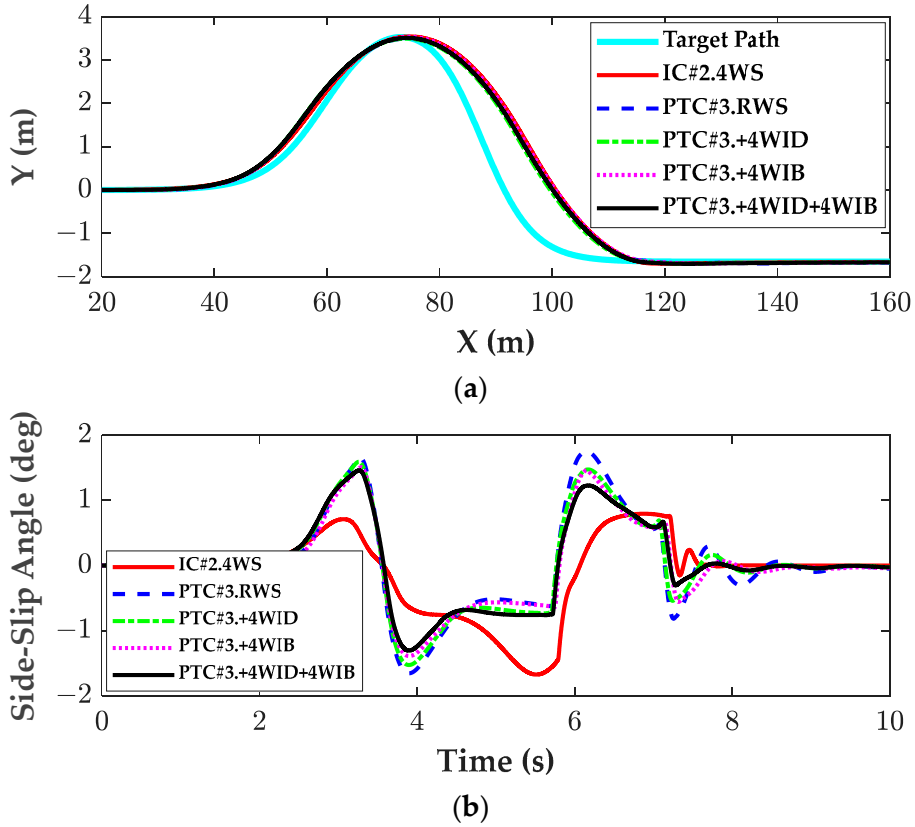

Figure 11. Simulation results with *IC*#2 and PTC#3. (**a**) Trajectories. (**b**) Side-slip angles.

5. Conclusions

The aim of this study is to compare three types of coordinated controllers, i.e., PTC#1, PTC#2, and PTC#3 on low-friction roads. With the state-space model derived from a 2-DOF bicycle model and a target path, the three controllers were designed. To calculate the steering angles and yaw moment control, LQR was designed. For yaw rate tracking, SMC was designed. As an actuator for path tracking and yaw moment generation, FWS, RWS, 4WS, 4WID, and 4WIB were adopted. For yaw moment distribution or control allocation with the multiple actuators, the WLS-based method was applied. To check the path-tracking performance of each controller, a simulation was carried out using the vehicle simulation package CarSim. For simulation, double lane change for collision avoidance was adopted as a test scenario. From the simulation results, it was shown that PTC#2 is superior to PTC#1 and PTC#3, and that there are little differences among PTC#1 and PTC#3. For this reason, PTC#3 is not recommended as a path-tracking controller. However, there are small differences between PTC#1 and PTC#2 in terms of path-tracking performance except for the peak's lateral offset and the settling delay. PTC#1 requires a two-level controller and PTC#2 uses a three-level control structure. Moreover, IC#1 and IC#2 of PTC#1 do not require yaw rate tracking and control allocation. As provided in Section 2, the yaw rate tracking controller and control allocation require several variables that are difficult to measure. Because the simplest has been shown to be the best, it is recommended that PTC#1 is the best controller for coordinated control of path tracking and vehicle stability control on low-friction roads. This conclusion was also drawn in the previous research [12]. As pointed out in the previous research, there are no significant differences among actuator combinations [13]. In other words, FWS or 4WS itself is quite enough for coordinated control of path tracking and vehicle stability control. Another conclusion from the simulation results is that it is important to tune the controller gain or select a controller type that is effective on both high- and low-friction roads.

Author Contributions: M.P. conceptualized the main idea and designed this study. S.Y. participated in formulating the idea, as well as validating the proposed method and results. S.Y. implemented the methodology and drafted the manuscript. All authors have read and agreed to the published version of the manuscript.

Funding: This work was supported by the Ministry of Trade, Industry and Energy (MOTIE, Korea). (Project Name: Development of Fail Operation technology in Lv.4 autonomous driving systems/Project Number: 20018055). Also, this work is supported by the Korea Agency for Infrastructure Technology Advancement (KAIA) grant funded by the Ministry of Land, Infrastructure and Transport (Grant RS-2021-KA160501).

Data Availability Statement: Not applicable.

Conflicts of Interest: The authors declare no conflict of interest.

Nomenclature

4WS	Four-wheel steering
4WIB	Four-wheel independent braking
4WID	Four-wheel independent drive
FWS	Front-wheel steering
MASSA	Maximum absolute side-slip angle
RWS	Rear-wheel steering
WLS	Weighted least square
C_f, C_r	Cornering stiffness of front and rear tires (N/rad)
e_y, e_φ	Lateral offset error (m) and heading error (rad)
F_{xi}, F_{zi}	Longitudinal and vertical tire forces of *i*-th wheel (N)
F_{yf}, F_{yr}	Front and rear lateral tire forces in the 2-DOF bicycle model (N)
$h(\omega)$	A function of rotor speed representing the capacity curve of an electric motor
I_z	Yaw moment of inertial (kg·m^2)
J_i	LQ objective function for the input configuration *IC#i*
K_i	Gain matrix of LQR for input configuration IC#*i*
L_p	Lookahead distance (m)
LWLC	Lower-level controller
l_f, l_r	Distance from cog to front and rear axles (m)
m	Vehicle total mass (kg)
MDLC	Middle-level controller
$OS\%$	Percentage of overshoot in the lower lane of the target path
p	Vector used for the equality constraint in the WLS-based method
q	Vector of tire forces as a solution of the WLS-based method
r_{wi}	Radius of *i*-th wheel (m)
T_{Bi}, T_{Di}	Braking and traction torques applied at *i*-th wheel (N·m)
UPLC	Upper-level controller
t_f, t_r	Half of track widths of front and rear axles (m)
t_p	Preview time for lookahead distance
v_x, v_y	Longitudinal and lateral velocities of cog of a vehicle (m/s)
W	Weighting matrix of WLS-based method
$X(*)$, $Y(*)$	X- and y-positions of the point $*$ on the target path and vehicle trajectory
$Y_{ref}(\mathrm{X})$	y-position of the target path with respect to X
α_f, α_r	Tire slip angles of front and rear wheels (rad)
β	Side-slip angle of C.G. of a vehicle (rad) = $\tan^{-1}(v_y/v_x) \approx (v_y/v_x)$
δ_f, δ_r	Front and rear steering angles (rad)
ε	10^{-4} used as a virtual weight in WLS-based method
ΔF_{xi}	Control longitudinal and lateral forces generated by an actuator (N)
ΔM_z	Control yaw moment as a control input in LQR (N·m)
ΔX, ΔY	Differences between x- and y-positions at the peak points of the target path
ΔDX, ΔSX	Response and settling delays of vehicle trajectory with respect to target path
γ, γ_{ref}	Measured and referenced yaw rates (rad/s)
γ_s, γ_p, γ_d	Reference yaw rates obtained from steering angle and target path (rad/s)
ζ	Tuning parameter on relaxation term of equality constraint

χ	Curvature at a particular point on a target path.
κ	Virtual weight on the longitudinal and lateral tire forces
$\boldsymbol{\kappa}$	Vector of virtual weights
ζ_i	The maximum allowable value of i-th term in the LQ objective function
$\boldsymbol{\zeta}$	Vector of the maximum allowable values
φ	Heading angle of a vehicle
φ_d	Desired heading angle obtained with lookahead
$\Psi_{ref}(X)$	Heading angle of the target path with respect to X
μ	Tire-road friction coefficient
ω_i	Rotational speed of i-th wheel (rad/s)
ρ_i	Weight on i-th term in LQ objective function
τ	Time constant of the first-order system used for reference yaw rate
v_i	Ratio of reduction gear of i-th wheel

References

1. Montanaro, U.; Dixit, S.; Fallaha, S.; Dianatib, M.; Stevensc, A.; Oxtobyd, D.; Mouzakitisd, A. Towards connected autonomous driving: Review of use-cases. *Veh. Syst. Dyn.* **2019**, *57*, 779–814. [CrossRef]
2. Yurtsever, E.; Lambert, J.; Carballo, A.; Takeda, K. A survey of autonomous driving: Common practices and emerging technologies. *IEEE Access* **2020**, *8*, 58443–58469. [CrossRef]
3. Omeiza, D.; Webb, H.; Jirotka, M.; Kunze, M. Explanations in autonomous driving: A survey. *IEEE Trans. Intell. Transp. Syst.* **2022**, *23*, 10142–10162. [CrossRef]
4. Sorniotti, A.; Barber, P.; De Pinto, S. Path tracking for automated driving: A tutorial on control system formulations and ongoing research. In *Automated Driving*; Watzenig, D., Horn, M., Eds.; Springer: Cham, Switzerland, 2017.
5. Amer, N.H.; Hudha, H.Z.K.; Kadir, Z.A. Modelling and control strategies in path tracking control for autonomous ground vehicles: A review of state of the art and challenges. *J. Intell. Robot. Syst.* **2017**, *86*, 225–254. [CrossRef]
6. Paden, B.; Cap, M.; Yong, S.Z.; Yershov, D.; Frazzoli, E. A survey of motion planning and control techniques for self-driving urban vehicles. *IEEE Trans. Intell. Veh.* **2016**, *1*, 33–55. [CrossRef]
7. Bai, G.; Meng, Y.; Liu, L.; Luo, W.; Gu, Q.; Liu, L. Review and comparison of path tracking based on model predictive control. *Electronics* **2019**, *8*, 10. [CrossRef]
8. Yao, Q.; Tian, Y.; Wang, Q.; Wang, S. Control strategies on path tracking for autonomous vehicle: State of the art and future challenges. *IEEE Access* **2020**, *8*, 161211–161222. [CrossRef]
9. Rokonuzzaman, M.; Mohajer, N.; Nahavandi, S.; Mohamed, S. Review and performance evaluation of path tracking controllers of autonomous vehicles. *IET Intell. Transp. Syst.* **2021**, *15*, 646–670. [CrossRef]
10. Stano, P.; Montanaro, U.; Tavernini, D.; Tufo, M.; Fiengo, G.; Novella, L.; Sorniotti, A. Model predictive path tracking control for automated road vehicles: A review. *Annu. Rev. Control* **2022**, *55*, 194–236. [CrossRef]
11. Jeong, Y.; Yim, S. Integrated path tracking and lateral stability control with four-wheel independent steering for autonomous electric vehicles on low friction roads. *Machines* **2022**, *10*, 650. [CrossRef]
12. Lee, J.; Yim, S. Comparative study of path tracking controllers on low friction roads for autonomous vehicles. *Machines* **2023**, *11*, 403. [CrossRef]
13. Park, M.; Yim, S. Comparative study on effects of input configurations of linear quadratic controller on path tracking performance under low friction condition. *Actuators* **2023**, *12*, 151. [CrossRef]
14. Ahangarnejad, A.H.; Radmehr, A.; Ahmadian, M. A review of vehicle active safety control methods: From antilock brakes to semiautonomy. *J. Vib. Control* **2021**, *27*, 1683–1712. [CrossRef]
15. Zhang, L.; Zhang, Z.; Wang, Z.; Deng, J.; Dorrell, D.G. Chassis coordinated control for full x-by-wire vehicles—A review. *Chin. J. Mech. Eng.* **2021**, *34*, 42. [CrossRef]
16. Peng, H.; Chen, X. Active safety control of x-by-wire electric vehicles: A survey. *SAE Int. J. Veh. Dyn. Stab. NVH* **2022**, *6*, 115–133. [CrossRef]
17. Indu, K.; Kumar, M.A. Electric vehicle control and driving safety systems: A review. *IETE J. Res.* **2023**, *6*, 482–498. [CrossRef]
18. Yim, S. Comparison among active front, front independent, 4-wheel and 4-wheel independent steering systems for vehicle stability control. *Electronics* **2020**, *9*, 798. [CrossRef]
19. Nah, J.; Yim, S. Vehicle stability control with four-wheel independent braking, drive and steering on in-wheel motor-driven electric vehicles. *Electronics* **2020**, *9*, 1934. [CrossRef]
20. Hang, P.; Chen, X.; Luo, F. *Path-Tracking Controller Design for a 4WIS and 4WID Electric Vehicle with Steer-by-Wire System (No. 2017-01-1954)*; SAE Technical Paper: Warrendale, PA, USA, 2017.
21. Guo, J.; Luo, Y.; Li, K. An adaptive hierarchical trajectory following control approach of autonomous four-wheel independent drive electric vehicles. *IEEE Trans. Intell. Transp. Syst.* **2018**, *19*, 2482–2492. [CrossRef]

22. Guo, J.; Luo, Y.; Li, K.; Dai, Y. Coordinated path-following and direct yaw-moment control of autonomous electric vehicles with sideslip angle estimation. *Mech. Syst. Signal Process.* **2018**, *105*, 183–199. [CrossRef]
23. Hang, P.; Chen, X.; Luo, F. LPV/H_∞ controller design for path tracking of autonomous ground vehicles through four-wheel steering and direct yaw-moment control. *Int. J. Automot. Technol.* **2019**, *20*, 679–691. [CrossRef]
24. Peng, H.; Wang, W.; An, Q.; Xiang, C.; Li, L. Path tracking and direct yaw moment coordinated control based on robust MPC with the finite time horizon for autonomous independent-drive vehicles. *IEEE Trans. Veh. Technol.* **2020**, *69*, 6053–6066. [CrossRef]
25. Wang, Y.; Shao, Q.; Zhou, J.; Zheng, H.; Chen, H. Longitudinal and lateral control of autonomous vehicles in multi-vehicle driving environments. *IET Intell. Transp. Syst.* **2020**, *14*, 924–935. [CrossRef]
26. Wu, H.; Li, Z.; Si, Z. Trajectory tracking control for four-wheel independent drive intelligent vehicle based on model predictive control and sliding mode control. *Adv. Mech. Eng.* **2021**, *13*, 16878140211045142. [CrossRef]
27. Xiang, C.; Peng, H.; Wang, W.; Li, L.; An, Q.; Cheng, S. Path tracking coordinated control strategy for autonomous four in-wheel-motor independent-drive vehicles with consideration of lateral stability. *Proc. Inst. Mech. Eng. Part D J. Automob. Eng.* **2021**, *235*, 1023–1036. [CrossRef]
28. Barari, A.; Afshari, S.S.; Liang, X. Coordinated control for path-following of an autonomous four in-wheel motor drive electric vehicle. *Proc. Inst. Mech. Eng. Part C J. Mech. Eng. Sci.* **2022**, *236*, 6335–6346. [CrossRef]
29. Wang, W.; Zhang, Y.; Yang, C.; Qie, T.; Ma, M. Adaptive model predictive control-based path following control for four-wheel independent drive automated vehicles. *IEEE Trans. Intell. Transp. Syst.* **2022**, *23*, 14399–14412. [CrossRef]
30. Jin, L.; Gao, L.; Jiang, Y.; Chen, M.; Zheng, Y.; Li, K. Research on the control and coordination of four-wheel independent driving/steering electric vehicle. *Adv. Mech. Eng.* **2017**, *9*, 1687814017698877. [CrossRef]
31. Ren, Y.; Zheng, L.; Khajepour, A. Integrated model predictive and torque vectoring control for path tracking of 4-wheeldriven autonomous vehicles. *IET Intell. Transp. Syst.* **2019**, *13*, 98–107. [CrossRef]
32. Guo, L.; Ge, P.; Yue, M.; Li, J. Trajectory tracking algorithm in a hierarchical strategy for electric vehicle driven by four independent in-wheel motors. *J. Chin. Inst. Eng.* **2020**, *43*, 807–818. [CrossRef]
33. Ahn, T.; Lee, Y.; Park, K. Design of integrated autonomous driving control system that incorporates chassis controllers for improving path tracking performance and vehicle stability. *Electronics* **2021**, *10*, 144. [CrossRef]
34. Liang, Y.; Li, Y.; Zheng, L.; Yu, Y.; Ren, Y. Yaw rate tracking-based path-following control for four-wheel independent driving and four-wheel independent steering autonomous vehicles considering the coordination with dynamics stability. *Proc. Inst. Mech. Eng. Part D J. Automob. Eng.* **2021**, *235*, 260–272. [CrossRef]
35. Xie, J.; Xu, X.; Wang, F.; Tang, Z.; Chen, L. Coordinated control based path following of distributed drive autonomous electric vehicles with yaw-moment control. *Control Eng. Pract.* **2021**, *106*, 104659. [CrossRef]
36. Tong, Y.; Jing, H.; Kuang, B.; Wang, G.; Liu, F.; Yang, Z. Trajectory tracking control for four-wheel independently driven electric vehicle based on model predictive control and sliding model control. In Proceedings of the 2021 5th CAA International Conference on Vehicular Control and Intelligence (CVCI), Tianjin, China, 29–31 October 2021.
37. Du, Q.; Zhu, C.; Li, Q.; Tian, B.; Li, L. Optimal path tracking control for intelligent four-wheel steering vehicles based on MPC and state estimation. *Proc. Inst. Mech. Eng. Part D J. Automob. Eng.* **2022**, *236*, 1964–1976. [CrossRef]
38. Sun, X.; Wang, Y.; Hu, W.; Cai, Y.; Huang, C.; Chen, L. Path tracking control strategy for the intelligent vehicle considering tire nonlinear cornering characteristics in the PWA form. *J. Frankl. Inst.* **2022**, *359*, 2487–2513. [CrossRef]
39. Jeong, Y.; Yim, S. Path tracking control with four-wheel independent steering, driving and braking systems for autonomous electric vehicles. *IEEE Access* **2022**, *10*, 74733–74746. [CrossRef]
40. Hu, H.; Bei, S.; Zhao, Q.; Han, X.; Zhou, D.; Zhou, X.; Li, B. Research on trajectory tracking of sliding mode control based on adaptive preview time. *Actuators* **2022**, *11*, 34. [CrossRef]
41. Tarhini, F.; Talj, R.; Doumiati, M. Adaptive look-ahead distance based on an intelligent fuzzy decision for an autonomous vehicle. In Proceedings of the 2023 IEEE Intelligent Vehicles Symposium (IV), Anchorage, AK, USA, 4–7 June 2023.
42. Wong, H.Y. *Theory of Ground Vehicles*, 3rd ed.; John Wiley and Sons, Inc.: New York, NY, USA, 2001.
43. Rajamani, R. *Vehicle Dynamics and Control*; Springer: New York, NY, USA, 2006.
44. Bryson, A.E.; Ho, Y.C. *Applied Optimal Control*; Hemisphere: New York, NY, USA, 1975.
45. Wang, J.; Wang, R.; Jing, H.; Chen, N. Coordinated active steering and four-wheel independently driving/braking control with control allocation. *Asian J. Control* **2016**, *18*, 98–111. [CrossRef]
46. Rezaeian, A.; Zarringhalam, R.; Fallah, S.; Melek, W.; Khajepour, A.; Chen, S.-K.; Moshchuck, N.; Litkouhi, B. Novel tire force estimation strategy for real-time implementation on vehicle applications. *IEEE Trans. Veh. Technol.* **2015**, *64*, 2231–2241. [CrossRef]
47. Yim, S.; Choi, J.; Yi, K. Coordinated control of hybrid 4WD vehicles for enhanced maneuverability and lateral stability. *IEEE Trans. Veh. Technol.* **2012**, *61*, 1946–1950. [CrossRef]
48. Yim, S. Coordinated control with electronic stability control and active steering devices. *J. Mech. Sci. Technol.* **2015**, *29*, 5409–5416. [CrossRef]
49. Yakub, F.; Mori, Y. Comparative study of autonomous path-following vehicle control via model predictive control and linear quadratic control. *Proc. Inst. Mech. Eng. Part D J Automob. Eng.* **2015**, *229*, 1695–1714. [CrossRef]
50. Kim, H.H.; Ryu, J. Sideslip angle estimation considering short-duration longitudinal velocity variation. *Int. J. Automot. Technol.* **2011**, *12*, 545–553. [CrossRef]

51. National Highway Traffic Safety Administration. *FMVSS No. 126, Electronic Stability Control Systems: NHTSA Final Regulatory Impact Analysis*; National Highway Traffic Safety Administration: Washington, DC, USA, 2007.
52. Mechanical Simulation Corporation. *VS Browser: Reference Manual, The Graphical User Interfaces of BikeSim, CarSim, and TruckSim*; Mechanical Simulation Corporation: Ann Arbor, MI, USA, 2009.